

Supporting Information

Bonding Pathways of Gold Nanocrystals in Solution

Zainul Aabdin,^{1,2,3,4*} Jingyu Lu,^{1,2,3,4*} Xi Zhu,^{5*} Utkarsh Anand,^{1,2,3} N. Duane Loh,^{1,3}
Haibin Su,⁵ and Utkur Mirsaidov^{1,2,3,4}

1. Department of Physics, National University of Singapore, 2 Science Drive 3, Singapore, 117551
2. Graphene Research Centre, National University of Singapore, 6 Science Drive 2, Singapore, 117546
3. Centre for Bioimaging Sciences and Department of Biological Sciences, National University of Singapore, 14 Science Drive 4, Singapore, 117543
4. NUSNNI-Nanocore, 5A Engineering Drive 1, National University of Singapore, Singapore, 117411
5. Division of Materials Science, Nanyang Technological University, 50 Nanyang Avenue, Singapore, 639798

Correspondence: (UM: phyumm@nus.edu.sg)

Materials and Methods:

The liquid cell, micro-fabricated from 200 μm thick silicon wafers, has two 20 nm thick electron translucent silicon nitride (SiN_x) membrane windows with lateral dimensions of $\sim 20 \times 50 \mu\text{m}$. These membrane windows are separated with a $\sim 100 \text{ nm}$ spacer.¹ The SiN_x membranes are plasma cleaned before liquid cell assembly and also right before loading the solution to render the membrane surfaces hydrophilic. We loaded $\sim 400 \text{ nL}$ of aqueous precursor solution containing 1 mM of HAuCl_4 (Sigma Aldrich: Product#: 254169) and 1 mM of cetrimonium bromide (CTAB) surfactant (Sigma Aldrich: Product#: H9151) into the liquid cell to stabilize the shape of the nanocrystals. After sealing the loading pockets with a copper gasket, the liquid cell is inserted into the TEM using a specimen holder. Inside the TEM, the electron beam passes through the top and the bottom SiN_x membranes, and the aqueous solution layer sandwiched between these membranes. Movement in CTAB is stimulated by electron beam. Under the electron beam ($> 5000 \text{ e}/(\text{\AA}^2 \cdot \text{s})$) gold nanocrystals in aqueous CTAB solution move.^{2,3} Since CTAB binds favourable to high energy surface: (100)

and (110),^{4,5} we only consider bonding through (111) surfaces. The bonding angles are defined as the angle between (111) common lattice planes.

Image Processing:

Our segmentation algorithm is implemented in the Python programming language, distributed by Enthought Canopy (Version 1.3.0). In order to make the image background more uniform we reduce the illumination gradient. First, a blurred version, generated by applying a wide Gaussian filter with $\sigma = 20$ pixels, of the original image is subtracted from the original image to produce a new image with lesser illumination gradient. This image is then smoothened using a Gaussian filter ($\sigma = 8$ pixels), followed by a 2D median filter 20×20 pixel. After smoothing, an intensity gradient filter is applied on the image. Regions bounded by closed gradient lines are considered as particles, and the image is binarized, i.e. 1 if a pixel belongs to a particle, 0 otherwise. A 3D binary volume stack, where z direction represents time, is generated using the segmented image sequence, and a 1D Gaussian smoothing is performed along the z direction. Objects are now labelled across different time points based on their: (1) area (if the change in particle area between two consecutive frames is less than 10%, they are treated as same object); and (2) centroid position (if the change in particle centroid between two consecutive frames is less than 5 pixels, they are treated as same object). The labelled volume stack is now used to evaluate the area, perimeter, circularity and centroid position of the particle.

Neck growth between two nanoparticles during coherent bonding (Fig. S1) is quantified by first skeletonizing the binarized image⁶. This skeleton is then fitted to a straight line, which we approximate as the central line connecting the centres of the two nanoparticles. The width of the neck is then the length of the shortest line segment bound by two nanoparticles' boundary (in the neck region) which is also perpendicular to this central line.

Molecular Dynamics Simulation:

The molecular dynamics (MD) simulations are performed with the Verlet algorithm, the structures are coupled with the Nose-Hoover thermostat in the NVT ensemble (constant atom numbers, volume, and temperature) at 300 K.⁷ We use 1 fs as the integration time step for the equation of motion in the simulation. The embedded atom method (EAM)^{8,9} is implemented to describe the interatomic potential of Au atoms.¹⁰

Finite size effects of surface energy density:

We extend the discussion in the main text regarding Fig. 2. The surface energy density of gold is $\gamma_{\text{Au}(111)}=0.075 \text{ eV}/\text{\AA}^2$,¹¹ which leads to a total energy reduction on the two 777.55 \AA^2 (330 gold atoms) bonding nanocrystal surfaces of 120 eV. The surface tension is also related to the melting temperature¹² as: $\gamma = 3(N/V)dk_B T_m$ (here N - the number of atoms, V - volume, k_B - Boltzmann constant, d - inter-plane distance, and T_m – melting temperature of nanocrystals). Due to finite-size effects, the melting temperature of bulk gold ($T_m=1337 \text{ K}$) differs from that of 10 nm gold nanocrystals ($T_m=1200 \text{ K}$).¹³ Hence the average surface energy density for the latter is $0.067 \text{ eV}/\text{\AA}^2$. Thus the energy gained during bonding is $\sim 100 \text{ eV}$, which is very close to the energy gains computed in our MD simulations.

Nanocrystal Bonding:

Figure S1A shows the coherent bonding of two gold nanocrystals along [110] lattice direction ($t = 0.3 \text{ s}$) with the common (111) lattice plane indicated by orange dashed lines ($t = 8.5 \text{ s}$). Absence of splitting in the Fourier reflections (inset: $t = 15.3 \text{ s}$, orange circle) show that the final crystal is a single crystal and there are no persistent defects. The neck formed during the bonding of these two crystals is filled with gold atoms (Fig. S1A). Since the total projected area of two gold nanocrystals is preserved throughout the crystal bonding (Fig. S1B), we think that the growth of the neck at the bonding interface is due to the migration of the surface atoms into the neck area and not due to the gold ions in the solution. The neck width at the bonding interface as a function of time is plotted in Figure S1C.

A clear example of defect dynamics during the nanocrystal bonding is shown in Figure S2, where prior to bonding the (Fig. S2A: $t = 0.5 \text{ s}$) nanocrystals are misaligned by 24° . Defect is formed at the bonding interface (Fig. S2A-B, $t = 2.0 \text{ s}$). This process is followed by a realignment of (111) lattice planes (Fig. S2A-B: $t = 4.7 \text{ s}$, dashed orange lines), which results in several partial defects within the nanocrystal (Fig. S2A-B: $t = 4.7 \text{ s}$, black arrows). These defects then move towards nanocrystal's surface ($t = 7.9 \text{ s}$) to reduce the total energy of the system (Fig. S2A-B: $t = 4.7 \text{ s} - 7.9 \text{ s}$). However, it is also possible for defects to be pinned to a bonding interface between two nanocrystals with little or no movement (Fig. 1B and S3).

As we have discussed in the main text both coherent and defect-mediated bonding are energetically favourable (Fig. 2C and Fig. 3C), however, the attachment of nanocrystals with

the smaller misalignment angles is preferred compared to the larger misalignment angles (Fig. 4B). This is due to the pre-attachment realignment of two nanocrystals that reduce the misalignment angle between their common (111) lattice plane prior to attachment¹⁴ (Fig. S4: $t = 23.7$ s - 366.5 s). Finally, they attach at an angle of about 5° yielding a defect-free single crystalline nanoparticle (Fig. S4: $t = 388.0$ s).

Effect of Out of Plane Rotation on Bragg Spots during Bonding:

Bragg spot corresponding to lattice spacing a for a crystal of diameter d imaged in TEM remains visible through an angular width of $\theta \approx 0.65a/d$ as discussed in detail by J. Lu *et al.*³. For a gold nanocrystal with a diameter of 10 nm, visibility of Fourier reflections means that out of plane rotation of the crystal is small $\theta \approx 0.9^\circ$.

Supporting Figures:

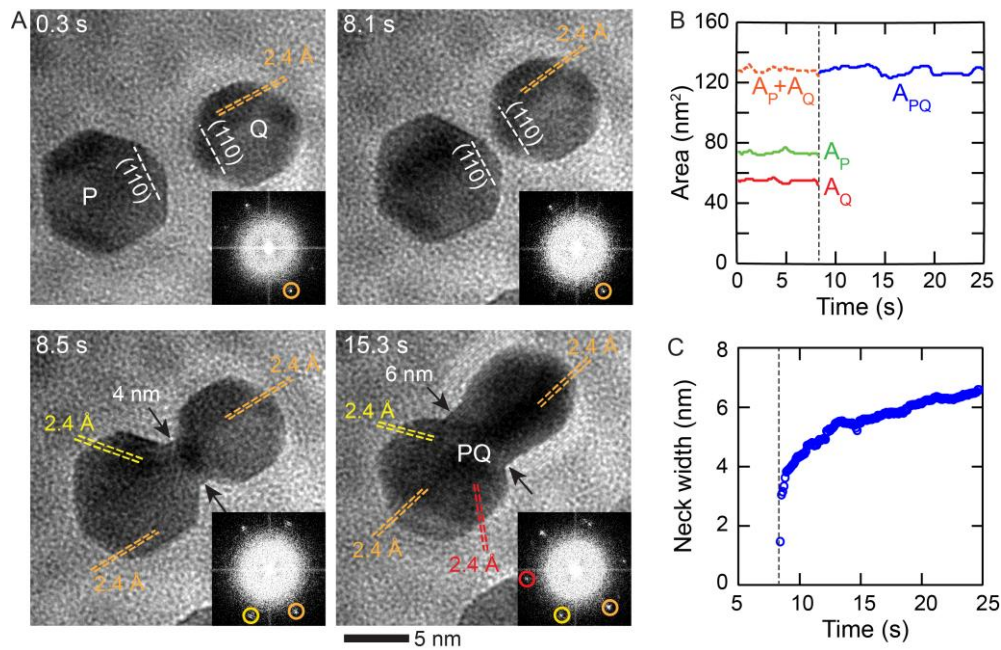


Figure S1. Coherent bonding of two nanocrystals. (A) Time-resolved high-resolution electron micrographs of bonding between two gold nanocrystals along [110] direction that share a common (111) lattice plane. No visible defects are formed at the bonding interface. (B) Projected area of the nanocrystal P (green curve, A_P), the nanocrystal Q (red curve, A_Q), their sum before (dashed orange curve, A_P+A_Q) and after bonding (blue curve, A_{PQ}) shows that the total area remains unchanged. (C) Projected neck width as a function of time. Nanocrystals contact at $t = 8.4$ s (dashed line).

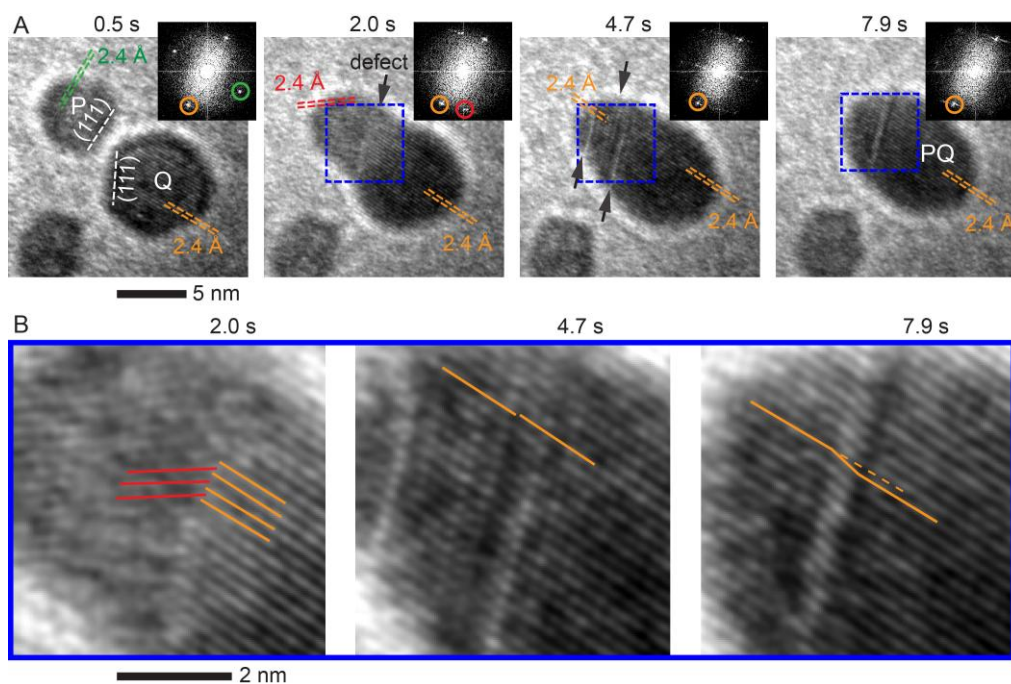


Figure S2. Defect-mediated bonding of two gold nanocrystals with transient defect formation at the bonding interface. (A) Time-resolved high-resolution electron micrographs of two gold nanocrystals bonding that are misoriented by 33° ($t = 0.5$ s). Defect is formed at the bonding interface (black arrow: $t = 2.0$ s), followed by realignment of (111) lattice planes which results in several partial defects (black arrows: $t = 4.7$ s). These defects then move within the nanocrystal towards its surface ($t = 7.9$ s). The splitting of the defect at the bonding interface into partial defects lowers the energy associated with the single large defect. Lattices fringes in (111) direction with 2.4 Å spacing are marked by parallel dashed lines with corresponding reflections circled in the Fourier transform. (B) Magnified view of the boxed area in (A). Red and orange lines mark (111) lattice fringes in each of two nanocrystals.

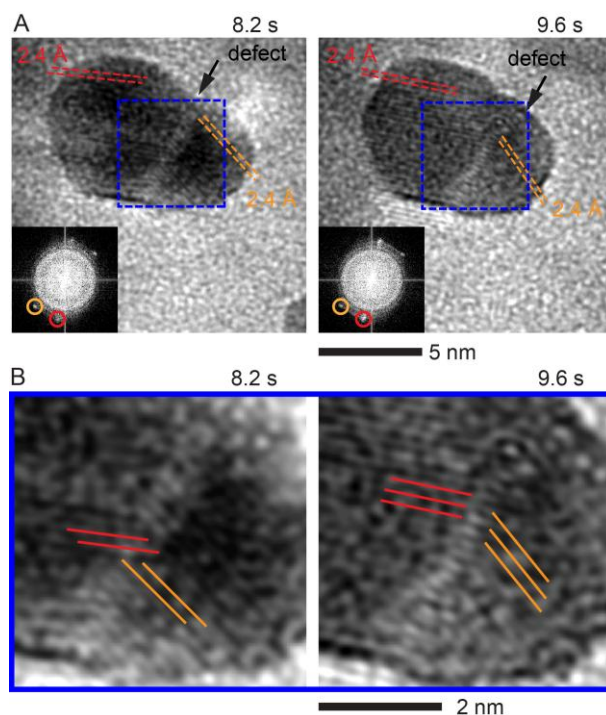


Figure S3. Defect-mediated attachment of gold nanocrystals shown in Figure 1B. (A) Time-resolved high-resolution electron images show that the defect (black arrow) appears at the bonding interface ($t = 8.2$ s). This defect is persistent and there is no realignment of the (111) lattice planes with time ($t = 9.6$ s). Corresponding reflections in the Fourier transforms are marked by red and orange circles. (Supporting Video S2) (B) Magnified view of the boxed area in (A). Red and orange lines mark (111) lattice fringes in each of two nanocrystals.

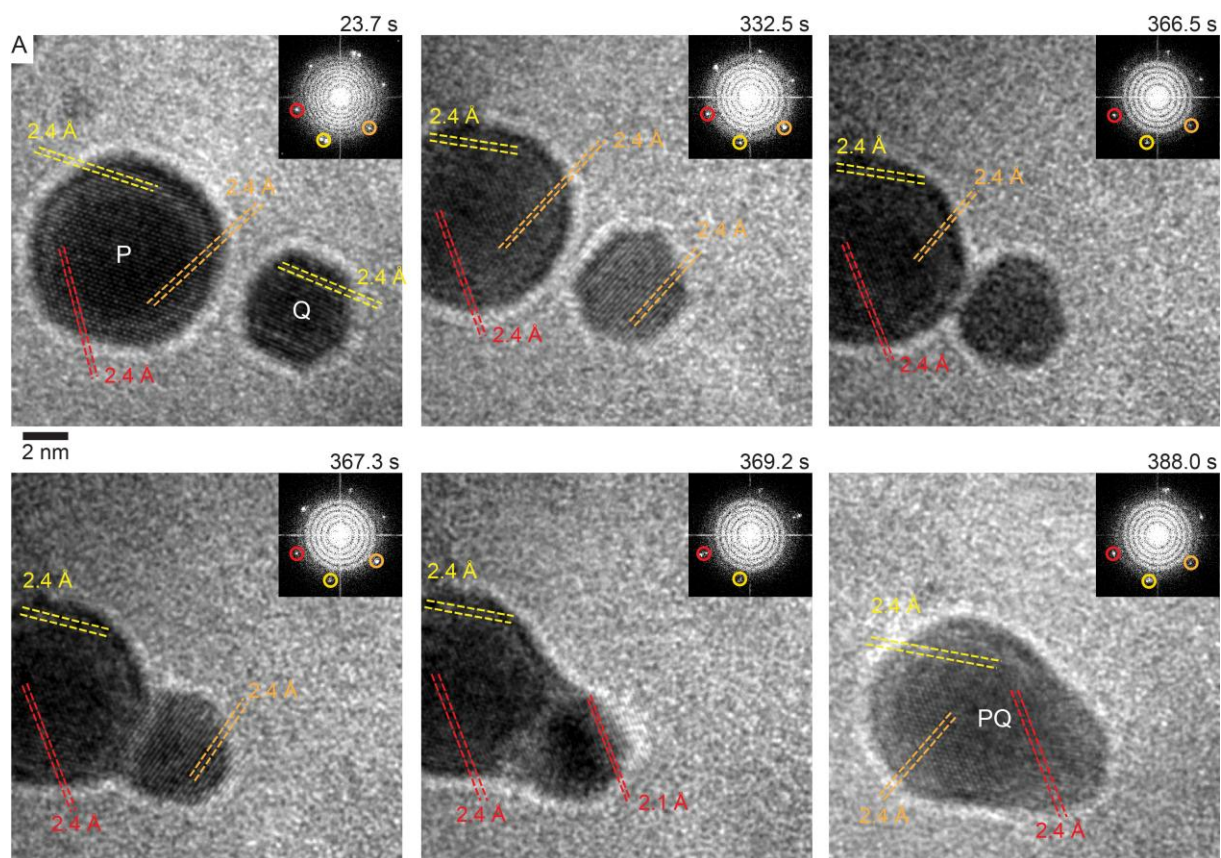


Figure S4. Realignment of gold nanocrystal leading to coherent bonding. Time-resolved high-resolution electron image show the realignment of the nanocrystals in an aqueous solution followed by defect-free coherent bonding through a common (111) lattice plane. Lattice fringes and corresponding reflections of the image are marked with dashed lines and circles of the same colour respectively. All the Fourier reflections are either 2.4 Å or 2.1 Å corresponding to (111) and (200) lattice spacing of a crystalline gold respectively (Supporting Video S4).

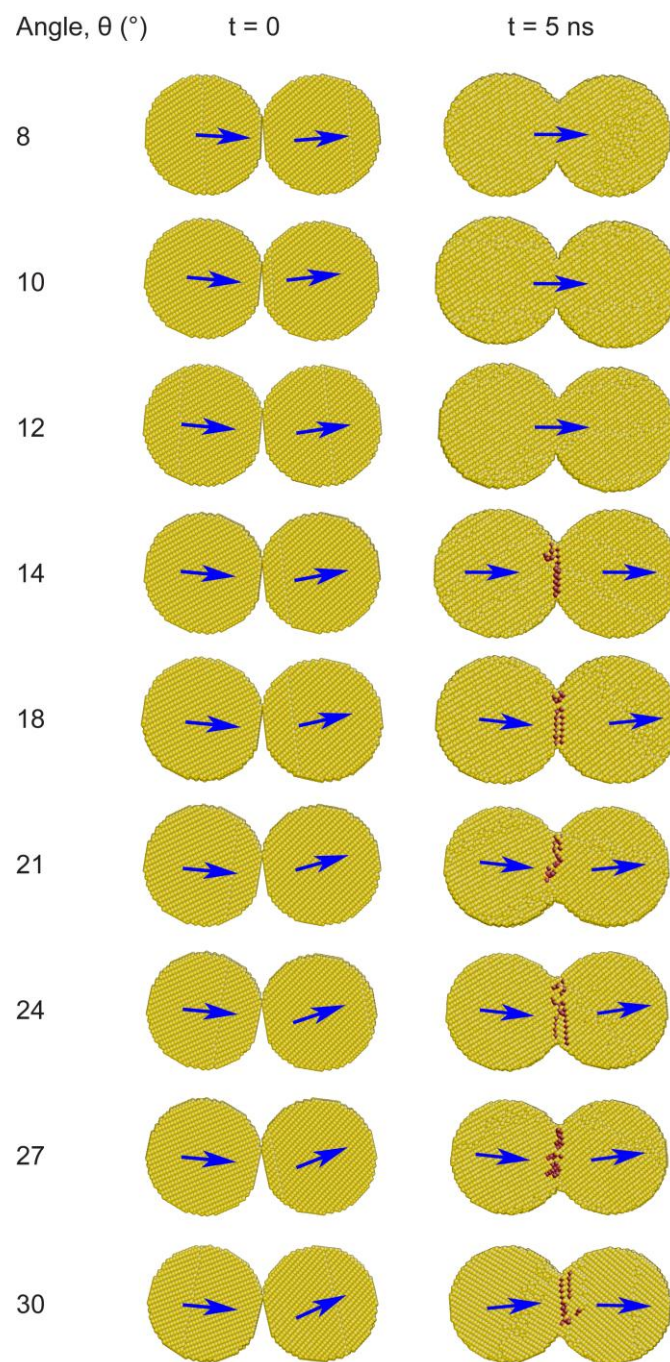


Figure S5. MD based structural evaluation of nanocrystal bonding at different attachment angles. Defect-free coherent bonding is observed for attachment angles smaller than 14° . Defect-mediated bonding is observed for 14° or greater. Red spheres represent gold atoms at defect sites distinct from rest of the crystalline gold atoms (yellow spheres). Arrows indicate $[111]$ direction. Here angles are measured between (111) lattice planes of two nanocrystals at contact.

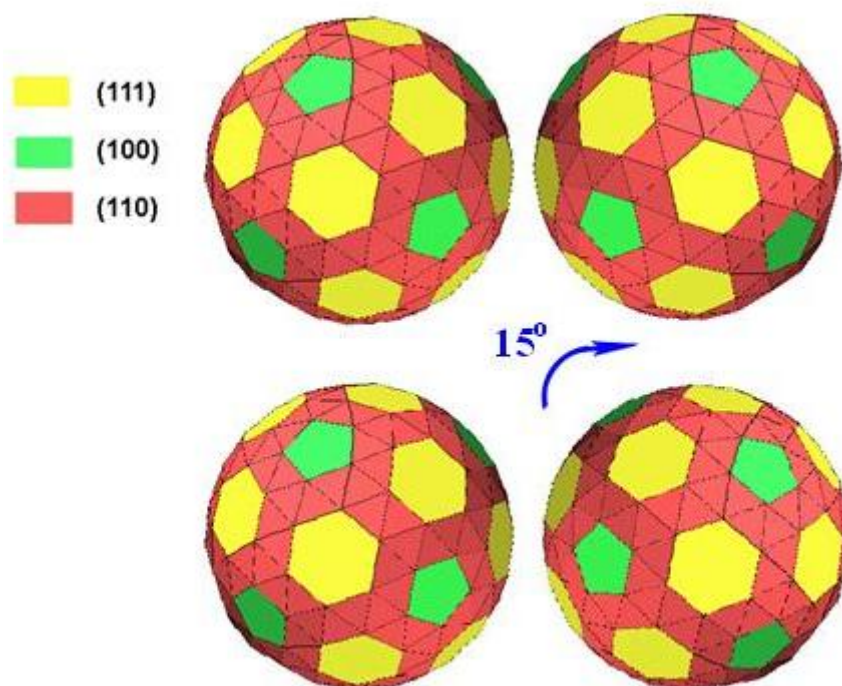


Figure S6. The facet orientations in the vicinity of junction for perfect alignment and 15° misalignment. The top panel shows the perfect aligned case when the angle between (111) faces of two gold nanocrystals is 0°. The bottom panel shows when the angle between (111) faces is 15°, the junction consists of (111) face of left nanocrystal facing (110) face of right nanocrystal.

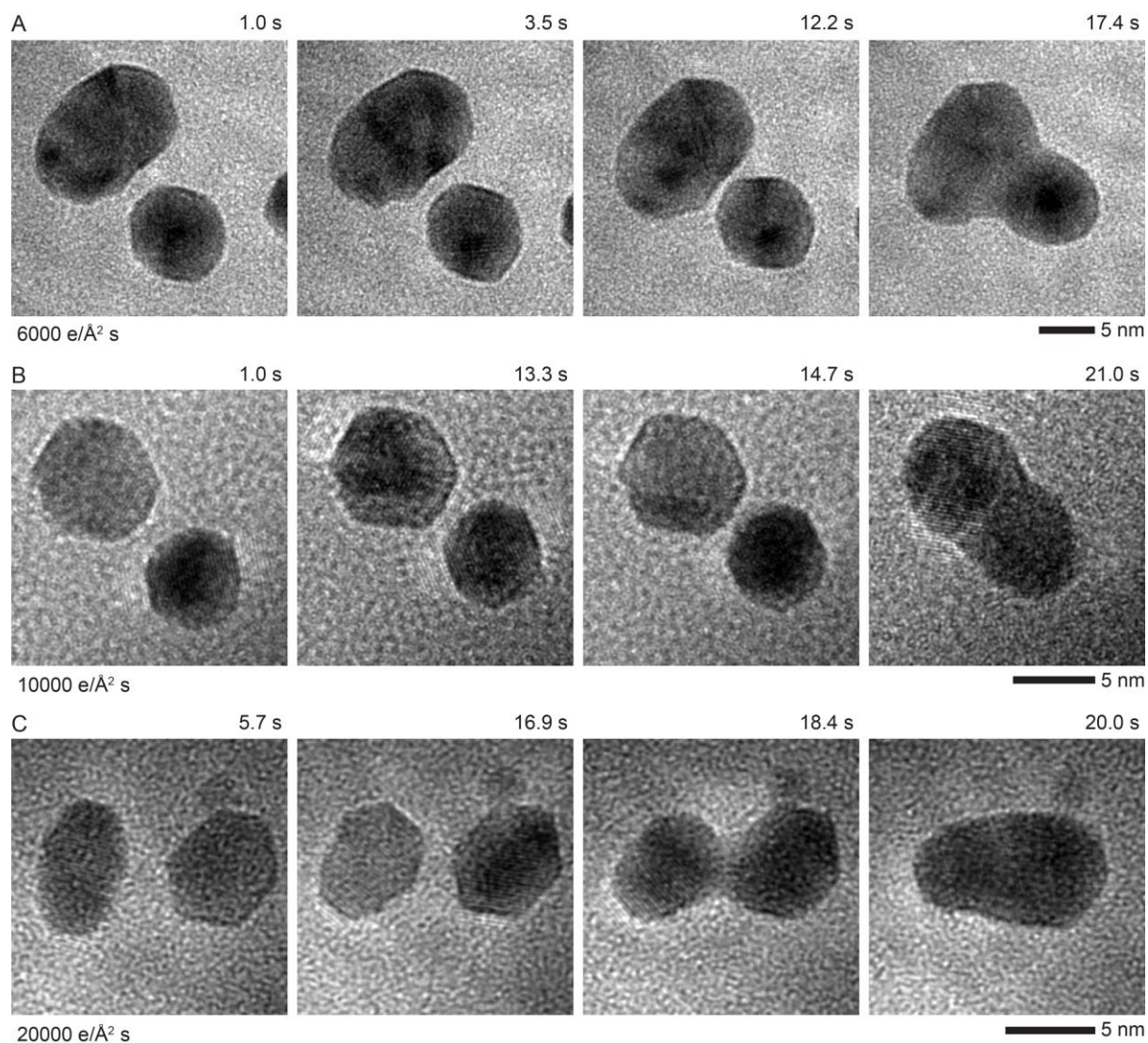


Figure S7. Nanocrystal bonding imaged at different electron doses. Bonding of nanocrystals imaged with (A) 6000 $\text{e}/\text{\AA}^2 \text{ s}$, (B) 10000 $\text{e}/\text{\AA}^2 \text{ s}$, and (C) 20000 $\text{e}/\text{\AA}^2 \text{ s}$ dose rate. Entire attachment and bonding process occurs within 20 s for all three cases.

Supporting Videos Captions:

Video S1: *In-situ* TEM movie of coherent bonding between two gold nanocrystals in aqueous solution. The misalignment Gold nanocrystals share a common (111) lattice plane and they contact along [111] direction with $\sim 9^\circ$. The Fourier transforms of the frames show the rotation dynamics of nanocrystals before and after bonding.

Video S2: *In-situ* TEM movie of defect-mediated bonding between two gold nanocrystals in aqueous solution. Defects are formed at their bonding interface. Nanocrystals' (111) lattice planes are misaligned by 32° before bonding. The Fourier transforms of the frames show the rotation dynamics of each nanocrystals before and after bonding.

Video S3: A mixed case: coherent and defect-mediated bonding between three gold nanocrystals in aqueous solution imaged by *in-situ* TEM. Top two gold nanocrystals share a common (111) lattice plane, and their bonding is defect-free. The newly formed top nanocrystal and bottom nanocrystal share uncommon (111) and (200) lattice planes. This results in defect formation at the bonding interface. The Fourier transforms of the frames show the rotation dynamics of nanocrystals before and after bonding.

Video S4: *In-situ* TEM movie of nanocrystal realignment followed by coherent bonding in aqueous solution. Nanocrystals' (111) lattice planes are misaligned by an angle of 5° just before the bonding. The Fourier transforms of the frames show the rotation dynamics of nanocrystals before and after bonding.

Supporting References:

- (1) Mirsaidov, U. M.; Zheng, H.; Bhattacharya, D.; Casana, Y.; Matsudaira, P. *Proc. Natl. Acad. Sci.* **2012**, *109*, 7187–7190.
- (2) Liu, Y.; Lin, X.-M.; Sun, Y.; Rajh, T. *J. Am. Chem. Soc.* **2013**, *135*, 3764–3767.
- (3) Lu, J.; Aabdin, Z.; Loh, N. D.; Bhattacharya, D.; Mirsaidov, U. *Nano Lett.* **2014**, *14*, 2111–2115.
- (4) Chen, H. M.; Liu, R.-S.; Tsai, D. P. *Cryst. Growth Des.* **2009**, *9*, 2079–2087.
- (5) Wang, L.; Chen, X.; Zhan, J.; Chai, Y.; Yang, C.; Xu, L.; Zhuang, W.; Jing, B. *J. Phys. Chem. B* **2005**, *109*, 3189–3194.
- (6) Van der Walt, S.; Schönberger, J.; Nunez-Iglesias, J.; Boulogne, F.; Warner, J.; Yager, N.; Gouillart, E. *PeerJ PrePrints 2*: **2014**, e336v2.
- (7) Hoover, W. G. *Phys. Rev. A* **1985**, *31*, 1695–1697.
- (8) Foiles, S. M.; Baskes, M. I.; Daw, M. S. *Phys. Rev. B* **1986**, *33*, 7983–7991.
- (9) Zhou, X. W.; Johnson, R. A.; Wadley, H. N. G. *Phys. Rev. B* **2004**, *69*, 144113.
- (10) Grouchko, M.; Roitman, P.; Zhu, X.; Popov, I.; Kamysny, A.; Su, H.; Magdassi, S. *Nat. Commun.* **2014**, *5*, 2994.
- (11) Grochola, G.; Russo, S. P.; Snook, I. K. *J. Chem. Phys.* **2005**, *123*, 204719.
- (12) Weale, R. A. *Nature* **1951**, *168*, 343.
- (13) Buffat, P.; Borel, J. *Phys. Rev. A* **1976**, *13*, 2287–2298.
- (14) Li, D.; Nielsen, M. H.; Lee, J. R. I.; Frandsen, C.; Banfield, J. F.; Yoreo, J. J. D. *Science* **2012**, *336*, 1014–1018.